

Photon energy reconstruction with the MEG II liquid xenon calorimeter

Kensuke Yamamoto^{1,*}, Sei Ban¹, Lukas Gerritzen¹, Toshiyuki Iwamoto¹, Satoru Koboyashi¹, Ayaka Matsushita¹, Toshi-nori Mori¹, Rina Onda¹, Wataru Ootani¹, and Atsushi Oya¹

¹ICEPP, The University of Tokyo, 7-3-1 Hongo, Bunkyo-ku, Tokyo 113-0033, Japan

Abstract. The MEG II experiment searches for a charged-lepton-flavour-violating $\mu \rightarrow e\gamma$ with the target sensitivity of 6×10^{-14} . A liquid xenon calorimeter with VUV-sensitive photosensors measures photon position, timing, and energy. This paper concentrates on the precise photon energy reconstruction with the MEG II liquid xenon calorimeter. Since a muon beam rate is $3\text{--}5 \times 10^7 \text{ s}^{-1}$, multi-photon elimination analysis is performed using waveform analysis techniques such as a template waveform fit. As a result, background events in the energy range of 48–58 MeV were reduced by 34%. The calibration of the energy scale of the calorimeter with several calibration sources is also discussed to achieve a high resolution of 1.8%.

1 Introduction

The charged-lepton-flavour-violating muon rare decay, $\mu \rightarrow e\gamma$, is strongly suppressed below a branching ratio of 10^{-54} in the Standard Model of particle physics considering neutrino oscillation. A branching ratio of $10^{-11}\text{--}10^{-14}$ is, however, predicted by new physics models beyond the Standard Model, such as supersymmetry [1]. The MEG II experiment aims to search for $\mu \rightarrow e\gamma$ with a sensitivity of approximately 6×10^{-14} using innovative high-resolution detectors and the most intense DC muon beam at Paul Scherrer Institut [2, 3] (Figure 1). Physics data-taking began in 2021 and is expected to continue until 2026. An upper limit on the branching ratio was set to 3.1×10^{-13} (90% C.L.) with a combination of the MEG full dataset and the MEG II first dataset [4].

Precise positron and photon measurements achieve high sensitivity by exploiting the kinematic difference be-

tween signal and background. The signal kinematics is a two-body decay: positron and photon are emitted back-to-back with monochromatic energy of 52.8 MeV simultaneously. Meanwhile, the dominant background is an accidental coincidence of positron and photon from different parent muons. The positron background source is the Michel decay ($\mu \rightarrow e\nu\nu$), and the photon background is generated by radiative muon decay (RMD; $\mu \rightarrow e\nu\nu\gamma$) and positron annihilation in flight (AIF) with electrons in the positron spectrometer. The number of the accidental background N_{acc} depends on the detector resolution σ :

$$N_{\text{acc}} \propto \sigma_{E_\gamma}^2 \cdot \sigma_{E_e} \cdot \sigma_{\Theta_{e\gamma}}^2 \cdot \sigma_{t_{e\gamma}}, \quad (1)$$

where $E_{\gamma(e)}$ is the photon (positron) energy, $\Theta_{e\gamma}$ is the opening angle between positron and photon, and $t_{e\gamma}$ is the time difference between them.

This paper will concentrate on the photon energy measurement for the data taken in 2021 and 2022. A liquid xenon calorimeter as a photon detector is introduced in Section 2. We then discuss analysis methods to realise high-resolution energy measurements in a high-intensity muon beam. Section 3 presents a multi-photon elimination algorithm. Section 4 discusses the calibration of the energy scale of the calorimeter.

2 Liquid xenon calorimeter

A liquid xenon (LXe) calorimeter plays a role in measuring photon position, timing, and energy in the MEG II experiment. This is a C-shape homogeneous calorimeter as shown in Figure 1 filled with 900 L of LXe to obtain a uniform response. The LXe has a lot of advantages in detecting 52.8 MeV photons; e.g. high stopping power (radiation length of 2.8 cm) and fast response (45 ns decay time). Since the scintillation light emitted from xenon is in the vacuum ultraviolet (VUV) region, 4760 VUV-sensitive photosensors are utilised for scintillation light

*e-mail: kensuke@icepp.s.u-tokyo.ac.jp

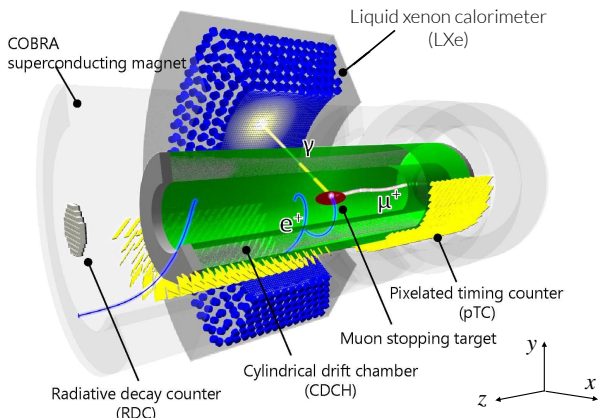


Figure 1. A sketch of the MEG II detector. Partially modified from Ref. [2].

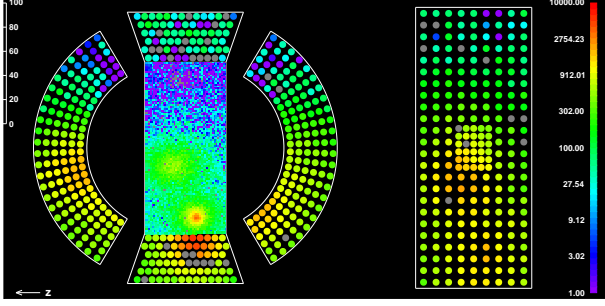


Figure 2. An unfolded view of the LXe calorimeter and scintillation light distribution. A colour bar represents the number of scintillation photons $N_{\text{pho},i}$ on the i -th photosensor. Two γ -rays impinge on the bottom half of the calorimeter.

detection. The photon entrance face is covered by 4092 Multi-Pixel Photon Counters (MPPCs) with the size of $1.5 \times 1.5 \text{ cm}^2$ [5] to achieve high granularity. The other faces are covered by 668 2-inch round-shape photomultiplier tubes (PMTs). The photosensors were calibrated to reconstruct the number of impinging scintillation photons on the i -th photosensor $N_{\text{pho},i}$ (Figure 2) as presented in Section 6.3 of Ref. [3]. The signal waveforms are read out with the DRS4 waveform digitiser [6] with a sampling frequency of 1.4 GSPS.

The photon energy is reconstructed by collecting all scintillation photons and converting them:

$$E_\gamma = N_{\text{sum}} \cdot S \cdot T(t) \cdot U(\vec{x}_\gamma), \quad (2)$$

$$N_{\text{sum}} = N_{\text{MPPC}} \cdot r_{\text{MPPC}}(t) + N_{\text{PMT}}, \quad (3)$$

where S is an energy scale conversion factor; $T(t)$ and $r_{\text{MPPC}}(t)$ are temporal variation correction functions; $U(\vec{x}_\gamma)$ is a non-uniformity correction function; and $N_{\text{MPPC(PMT)}}$ is the weighted sum of the number of scintillation photons $N_{\text{pho},i}$ detected by MPPCs (PMTs). The weighted N_{MPPC} and N_{PMT} sums are calculated, for single-photon events, via the multi-photon elimination algorithm discussed in Section 3. To achieve high resolution, the energy conversion factor S and the correction functions $T(t)$, $r_{\text{MPPC}}(t)$, and $U(\vec{x}_\gamma)$ must be calibrated as discussed in Section 4.

3 Multi-photon elimination

Multi-photon events deteriorate the energy resolution in a high-intensity muon beam. One of the multi-photon sources is two photons from AIF, both incident on the calorimeter. Furthermore, due to the high rate of the muon beam ($3\text{--}5 \times 10^7 \text{ s}^{-1}$), not only background but signal photons can be detected in accidental coincidence with low-energy photons in the DRS time window of about 700 ns, the so-called "pileup". The pileup event has to be unfolded to extract the information of each individual photon.

We first perform a peak search in the spatial distribution shown in Figure 2 to identify the multi-photon event candidates. We then analyse the MPPC and PMT summed waveforms with a template waveform fitting technique to

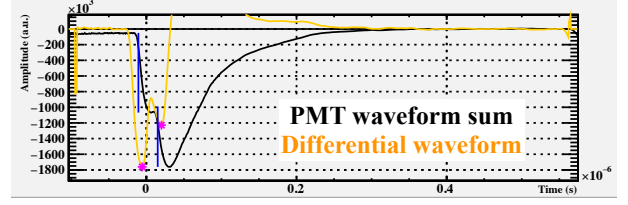


Figure 3. Multi-peak search in the PMT differential waveform in the same event as Figure 2. Magenta markers show the detected peaks in the differential waveform. Blue lines show the calculated peak time.

determine whether the detected multiple photons are coincident and to unfold multiple pulses in case the multiple photons are out of time. The template waveforms $f(\tau)$ were created by taking an average of the measured summed waveforms. Their fluctuation is expressed as a standard deviation at time τ $\sigma_f(\tau)$. The template waveform fit minimises a χ^2 defined as

$$\chi^2 = \sum_{\text{MPPC, PMT}} \int \frac{\left(V(\tau) - \sum_i^{n_{\text{pulse}}} f(\tau; A_i, t_i) \right)^2}{\sigma_f^2(\tau)} d\tau, \quad (4)$$

where $V(\tau)$ is observed MPPCs or PMTs summed waveform with position-dependent weights to optimise the N_{sum} resolution, and n_{pulse} is the number of fitted pulses. The amplitude A_i and timing t_i for the i -th pulse are fit parameters. Initial parameter sets of n_{pulse} , A_i , and t_i are calculated with three techniques, discussed in Section 3.1, before the waveform fit is performed.

3.1 Multi-photon detection techniques

The first step is to find pileup photons in the time domain from the summed waveform of photosensors. Here, we search for pileups from the PMT waveform, which is sharper than MPPC's. To make the waveform even sharper, we apply an additional algorithmic waveform processing to create a differential waveform dedicated to the pileup search. As shown in Figure 3, this processing makes waveform peaks (magenta markers) more distinguishable than those before the waveform processing. It, therefore, enables efficient detection of pileups. This technique can distinguish pulses with 15–20 ns and larger time differences according to the amplitude of the pulses.

The second step is clustering the photosensors based on the spatial distribution and analysing the summed waveforms of each cluster shown in Figure 4. This technique can distinguish distant photons with small time differences of a few to 20 ns, which are not distinguished by the differential waveform.

The last step is using the flash ADC signal used for the trigger whose time window is 1600 ns. The time window is more than twice as wide as the DRS time window (approximately 700 ns), though its sampling frequency is 80 MSPS. This signal enables us to obtain information on pulses coming before the DRS time window.

Figure 5 shows the unfolded pulses using the above-mentioned techniques. Once we have successfully unfolded the multiple pulses, we decide which pulses are

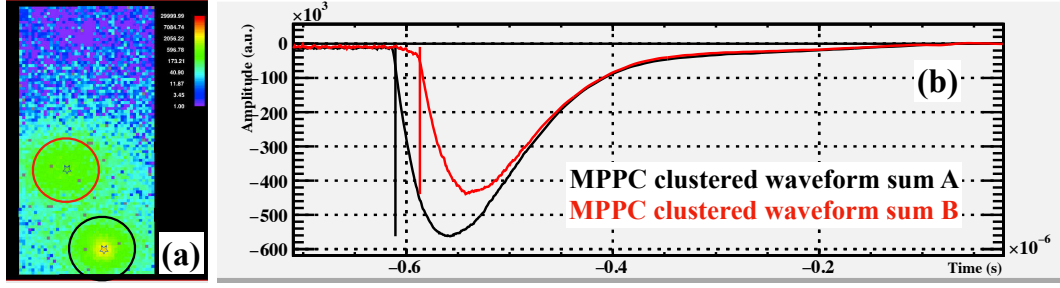


Figure 4. Multi-peak search based on the spatial distribution for the event of Figure 2. (a) Spatial distribution. (b) Summed waveforms of each cluster. The lines show the estimated pulse time.

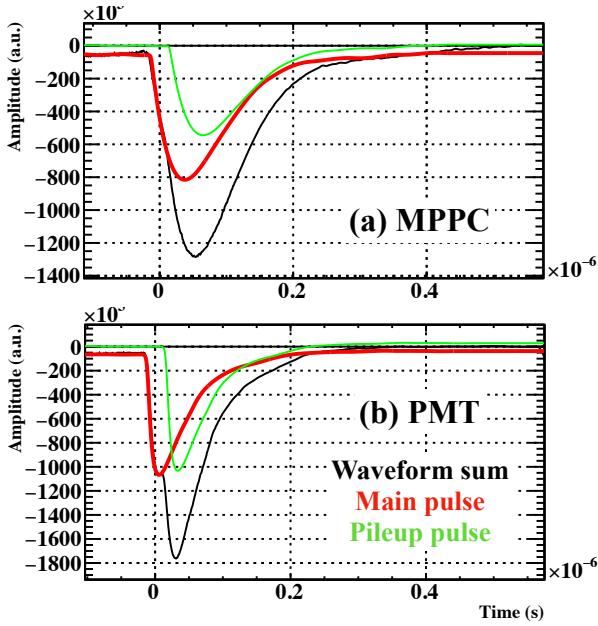


Figure 5. Unfolded multiple pulses for the event shown in Figures 2, 3, 4. The weighted sums N_{MPPC} and N_{PMT} are calculated by integrating out the waveform for the main pulse (red).

eliminated based on the results of the preceding position and timing reconstructions¹. For the event shown above, the position and timing were reconstructed for the black-circled photon in Figure 4. Therefore, the later pulse labelled the “pileup pulse” in Figure 5 is eliminated, and the first pulse (the “main pulse”) remains for the subsequent energy reconstruction. The weighted N_{MPPC} and N_{PMT} sums for the main pulse are calculated by integrating out the waveform of the main pulse.

3.2 Performance

Successfully unfolded events are used for the physics analysis. That is, events with coincident two photons and a fit failure are discarded from the analysis sample. The performance of the multi-photon elimination is evaluated based on a reduction of background events in the analysis region ($E_\gamma \in [48 \text{ MeV}, 58 \text{ MeV}]$) and the signal efficiency.

The number of background photons in 48–58 MeV was reduced by 34%. A clear drop around 52.8 MeV is

¹See Sections 6.4 and 6.5 of Ref. [3].

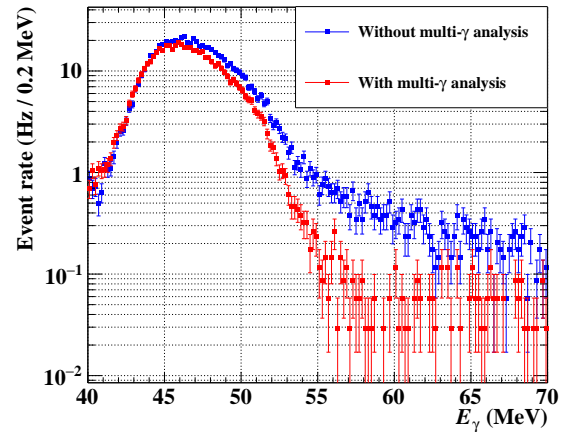


Figure 6. Background photon energy spectra with multi-photon elimination analysis (red) and without the analysis (blue) at a muon stopping rate of $3.4 \times 10^7 \text{ s}^{-1}$. An event drop below 45 MeV is derived from the trigger threshold based on photon energy.

seen in the energy spectrum thanks to the multi-photon elimination analysis (the red spectrum in Figure 6). The drop is essential to suppress the background events since the signal energy is monochromatic at 52.8 MeV.

The signal efficiency was evaluated as 95% based on the Monte Carlo simulation for the signal event. The inefficiency of 5% is mainly due to events where photons in an electromagnetic shower escape from the shower and develop a new shower far enough from the original shower. The new shower results in fake spatial on-timing peaks.

4 Energy scale calibration

The energy scale of the calorimeter has to be calibrated so as not to miss signal events and to achieve a resolution as high as possible for the whole data-taking period. The calibration for the 2021 data and the achieved energy resolution of 1.8% are described in Section 6.6 of Ref. [3]. This paper focuses on xenon impurity and its temporal evolution during the 2022 run, which is an additional difficulty from the 2021 run. This was due to the impure Xe which we added to fill the active volume up at the beginning. Purification was done in parallel with the data-taking to remove impurities.

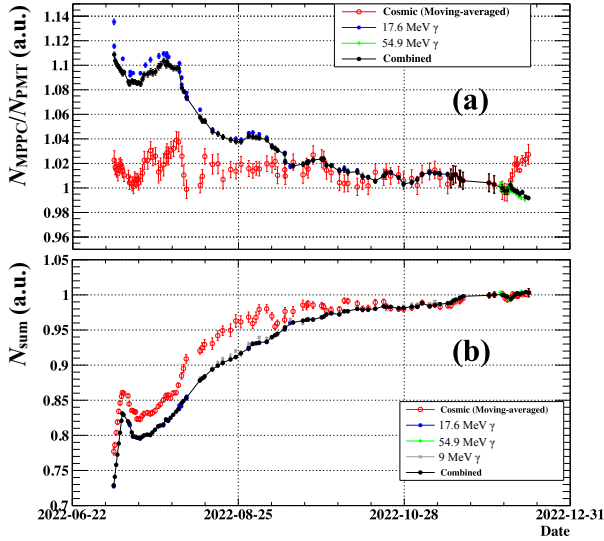


Figure 7. Temporal evolution of (a) a ratio of N_{MPPC} to N_{PMT} and (b) N_{sum} during the 2022 run. The correction function $r_{\text{MPPC}}(T)$ is a reciprocal of the combined history of $N_{\text{MPPC}}/N_{\text{PMT}}$ (N_{sum}).

The impurity reduced the transparency of LXe to scintillation light. It resulted in less scintillation light detection by PMTs for photons generated from the muon stopping target because most electromagnetic showers develop near the entrance face covered by MPPCs. Position-dependent weights on $N_{\text{pho},i}$ mentioned in Section 3, however, were optimised to make the N_{sum} peak width sharpest with 54.9 MeV photons from

$$\pi^- p \rightarrow \pi^0 n, \pi^0 \rightarrow \gamma\gamma$$

at the last of the 2022 run. We, therefore, need to calibrate the response difference between MPPCs and PMTs to keep the resolution using 17.6 MeV photons from ${}^7\text{Li}(p, \gamma){}^8\text{Be}$ reaction and cosmic rays penetrating the calorimeter as well as 54.9 MeV photons. Note that the 54.9 MeV-photon data was taken after the physics data-taking because it required a pion beam. Figure 7(a) shows a temporal evolution of the ratio of N_{MPPC} to N_{PMT} during the 2022 run. The ratio for photon data decreased as the Xe purity was recovered, as discussed above. Meanwhile, the ratio in cosmic-ray data was constant during the run because scintillation light was also generated near PMTs. The correction function r_{MPPC} is a reciprocal of the combined $N_{\text{MPPC}}/N_{\text{PMT}}$ history drawn in black in Figure 7(a).

The total detected scintillation light also decreased as impurities in LXe increased. It was calibrated also using 9 MeV photons from ${}^{58}\text{Ni}(n, \gamma){}^{59}\text{Ni}$ reaction as well as 17.6 MeV and 54.9 MeV photons and cosmic rays. Figure 7(b) shows the temporal evolution of the N_{sum} peak positions. We see a good agreement in the temporal evolutions between 9 MeV and 17.6 MeV photons. On the other hand, there is a discrepancy between photons and cosmic rays, which is not understood. We, however, relied on the photon data since the shower development should be similar to that of signal and background photons in a muon beam. The cosmic-ray data was used to connect the

peaks with 17.6 MeV and 54.9 MeV photons. The stability of the energy scale during the physics data-taking was assessed to be 0.2 % based on the standard deviation of reconstructed energy for 17.6 MeV photons after applying the correction function T .

5 Conclusion

The MEG II LXe calorimeter with 900L of LXe and 4760 VUV-sensitive photosensors measures photon position, timing, and energy. This paper focuses on photon energy reconstruction, discussing the multi-photon elimination algorithm and energy scale calibration.

The multi-photon elimination algorithm is performed to reconstruct single-photon energy in a high-intensity muon beam. Pileup photons are unfolded by the template waveform fit with three multi-photon detection techniques. The number of background events in the range of [48 MeV, 58 MeV] was reduced by 34 % in data while keeping the signal efficiency as high as 95 %.

We discuss the temporal evolution of the response difference between MPPCs and PMTs and of the energy scale due to Xe impurity. The stability during the physics data-taking was evaluated as 0.2 %. The calorimeter performance, such as the resolution, will be evaluated after the ongoing calibration. The physics analysis results with the 2021 and 2022 data will finally be released this year.

Acknowledgements

We are grateful for the support provided by PSI as the host laboratory. This work was supported by MEXT/JSPS KAKENHI Grant Numbers 21H04991, 22K21350, 24KJ0607, and JSPS Core-to-Core Program, A. Advanced Research Networks JPJSCCA20180004.

References

- [1] Y. Kuno, Y. Okada, Muon decay and physics beyond the standard model, *Reviews of Modern Physics* **73**, 151 (2001). [10.1103/RevModPhys.73.151](https://doi.org/10.1103/RevModPhys.73.151)
- [2] A.M. Baldini et al., The design of the MEG II experiment, *Eur. Phys. J. C* **78**, 380 (2018). [10.1140/epjc/s10052-018-5845-6](https://doi.org/10.1140/epjc/s10052-018-5845-6)
- [3] K. Afanaciev et al., Operation and performance of the MEG II detector, *Eur. Phys. J. C* **84**, 190 (2024). [10.1140/epjc/s10052-024-12415-3](https://doi.org/10.1140/epjc/s10052-024-12415-3)
- [4] K. Afanaciev et al., A search for $\mu^+ \rightarrow e^+ \gamma$ with the first dataset of the MEG II experiment, *Eur. Phys. J. C* **84**, 214 (2024). [10.1140/epjc/s10052-024-12416-2](https://doi.org/10.1140/epjc/s10052-024-12416-2)
- [5] K. Ieki et al., Large-area MPPC with enhanced VUV sensitivity for liquid xenon scintillation detector, *Nucl. Instrum. Meth. A* **925**, 148 (2019). [10.1016/j.nima.2019.02.010](https://doi.org/10.1016/j.nima.2019.02.010)
- [6] S. Ritt, The DRS chip: Cheap waveform digitizing in the GHz range, *Nucl. Instrum. Meth. A* **518** (2004). [10.1016/j.nima.2003.11.059](https://doi.org/10.1016/j.nima.2003.11.059)

